RSC Advances

PAPER

View Article Online
View Journal | View Issue

Cite this: *RSC Adv.*, 2022, **12**, 33688

Porous graphitic carbon nitride with high concentration of oxygen promotes photocatalytic H_2 evolution†

Ruokun Jia, *[a] Xueli Yu,[a] Xiaohang Yang,*[b] Xinzhe Wang, [a] Jiaming Yang,[a] Xuyang Huo[b] and Qiuju Qi[b]

Received 8th September 2022
Accepted 16th November 2022

DOI: 10.1039/d2ra05662c

rsc.li/rsc-advances

Porous structure design and the content regulation of heteroelements have been proved to be effective strategies to boost photocatalytic H_2 generation activity of graphitic carbon nitride (g-C_3N_4) based photocatalyst. Herein, a series of porous graphitic carbon nitride with high concentration of oxygen (g-C_3N_4–O) photocatalysts were synthesized *via in situ* polymerization process using colloidal SiO_2 as oxygen source. The content of oxygen within the g-C_3N_4–O photocatalysts could be tuned by adjusting the amount of added colloidal SiO_2 during the preparation procedure. The introduced oxygen replaced two-coordinated nitrogen atom, influencing band edge position and localized electron distribution, thereby enhancing visible light harvesting and photoelectric conversion. As a result, the g-C_3N_4–O photocatalyst with an optimal oxygen content (8.39 wt%) showed 10.5 fold enhancement in H_2 evolution rate compared to that of bulk g-C_3N_4, attributed to the porous structure and high concentration of incorporated oxygen.

Introduction

Limited fossil energy and serious environmental issues impel people to develop green and sustainable energy.[1] Hydrogen energy, as one of the most promising types of clean energy, could be directly prepared *via* water splitting driven by light or electricity and the combustion products are non-polluting to the environment.[2,3] Realizing the industrial production and application of hydrogen energy is a major demand for sustainable social development.[4] Water splitting under solar light irradiation by semiconductor photocatalysis technology appears to be an ideal strategy to generate H_2 energy.[5,6] The yield and industrialization prospects are determined by the visible light utilization ability and photoelectric conversion efficiency of the employed semiconductor photocatalysts.[7,8] Considering the problem of metal percolation of metal-based catalysts, graphitic carbon nitride (g-C_3N_4) is recognized as an appealing photocatalyst attributed to its metal-free properties, visible light response and sufficient reduction capacity.[9,10] Meanwhile, its excellent photo-stability and physicochemical stability are able to preserve long-term photocatalytic activity to satisfy industrial application requirements.[11] However, the inherent π-deficient conjugated characteristic of bulk g-C_3N_4 implies low charge density and carrier mobility, which are not favorable for the charge conduction.[12] The localization of π conjugated system leads to difficult spatial separation of photoexcited electrons and holes for g-C_3N_4.[13] Meanwhile, bulk g-C_3N_4 suffers from low surface areas and limited exposed active sites.[14] Hence, without modification, bulk g-C_3N_4 presentes poor photoelectric conversion efficiency and low photocatalytic H_2 production rate.

Incorporation of heteroelements to modulate the composition of g-C_3N_4 is effective to optimize its electronic properties and photocatalytic activity.[15,16] The introduced heteroelements could disturb local electron distribution of π conjugated system and expand delocalization to promote spatial separation of photoexcited charge carriers.[17,18] Generally, the selected heteroelements possess more valence electrons in comparison with C/N atoms, such as P, Cl, Br and I *etc.*[19–22] The introduced extra electrons would increase electron density of π conjugated system and thus elevate the conductivity, which was beneficial to improve transportation efficiency of photoinduced carriers.[23] For instance, after incorporation with iodine, the photocurrent and photocatalytic H_2 generation rate of g-C_3N_4–I significantly increased.[24] Another factor to consider is electronegativity, which could give much promotional effect on the electron distribution perturbation of π conjugated system.[25] O and F with high electronegativity are preferred candidates to optimize the electronic properties of g-C_3N_4.[26,27] Fluorination has been used to introduce F into g-C_3N_4 substrate by direct adding of HF/NH_4F into the typical condensation procedure. However, the process does not meet the requirements of environmental

[a]*College of Chemical Engineering, Northeast Electric Power University, Jilin 132012, China*

[b]*College of Biomedical Engineering, Jilin Medical University, Jilin 132013, China. E-mail: yxh4035@163.com; Fax: +86-0432-64560328; Tel: +86-0432-64560328*

† Electronic supplementary information (ESI) available. See DOI: https://doi.org/10.1039/d2ra05662c

protection due to the employment of harmful etchants.[28] Besides, the overlarge atomic radius of incorporated heteroelements is thermodynamically and geometrically difficult to substitute the C/N atom in the heptazine unites to form stable structure, which restrain the long-term stability and photocatalytic performance enhancement. Thereby, O with high electronegativity and comparable atom radius compared to C/N atoms is a recommended choice to modify g-C_3N_4.

In addition to heteroelement incorporation into g-C_3N_4 matrix, increase of surface area is desirable to elevate the overall photocatalytic performance. Researchers adopted surfactants, block polymers and ionic liquids as soft templates to synthesize microporous g-C_3N_4.[29–31] Mesoporous silica, silica nanoparticles and $CaCO_3$ nanosphere were selected as hard templates to prepared mesoporous g-C_3N_4.[32–34] The obtained porous architecture increased surface area, exposed active sites and promoted mass transfer, thus enhancing the photocatalytic performance of g-C_3N_4.[33] Therefore, simultaneously achievement of oxygen incorporation and textural pores within g-C_3N_4 is desirable to further improve the H_2 evolution performance.

In this work, we developed a facile approach to obtain porous g-C_3N_4 with high content of oxygen using colloidal SiO_2 as oxygen source. The concentration of introduced oxygen could be tuned by amount adjustment of added colloidal SiO_2 during the synthesis procedure. By substituting two-coordinated N atoms, the introduced O induced narrowed band gap and electron redistribution of HOMO/LUMO, thus contributing to extended visible light adsorption and promoted separation and transportation of photoexcited charge carriers. With respect to bulk g-C_3N_4, the obtained g-C_3N_4–O with an optimal oxygen content (8.39 wt%) exhibited 10.5 times enhancement in H_2 generation rate originating from mesoporous architecture formation and high oxygen content.

Experimental

Materials

Colloidal SiO_2 and Nafion were purchased from Sigma-Aldrich Company. Dicyandiamide (DCDA), ammonium bifluoride ($NH_4 \cdot HF_2$), ethanol and triethanolamine (TEOA) were purchased from Beijing Chemical Works. Chloroplatinic acid ($H_2PtCl_6 \cdot 6H_2O$) was purchased from Aladdin Company. Sodium sulfate (Na_2SO_4) was purchased from Shanghai Macklin Biochemical Technology Co., Ltd. All the reagents used in this work were analytical grade without further purification. Indium tin oxide (ITO) glass was purchased from Kaisheng Technology Co., Ltd. Deionized water (Millipore, 18.2 MΩ cm) was used throughout all the experiments.

Synthetic procedures

Bulk g-C_3N_4 was prepared *via* thermal polymerization of dicyandiamide (DCDA). The porous g-C_3N_4 with high concentration of oxygen (g-C_3N_4–O) were prepared *via in situ* thermal copolymerization using DCDA as g-C_3N_4 precursor and colloidal SiO_2 as oxygen source. Typically, a certain amount of colloidal SiO_2 and 1 g of DCDA were added into 2 mL of water. After stirring and sufficiently mixing, the mixtures were placed in a vacuum oven at 50 °C until the samples were completely dried. Then the white powders were calcined in a muffle furnace at 520 °C for 4 h with a heating rate of 10 °C min^{-1}. The resulting yellow powders were thoroughly ground in an agate mortar. Subsequently, the powders were washed with saturated $NH_4 \cdot HF_2$ solutions for 48 h. The obtained precipitates were washed by water for several times until the pH of the supernatant was neutral. The resulting brown products were then dried in a vacuum oven for further use. The amount of added colloidal SiO_2 during the preparation procedure were 500, 1000 and 2000 mg, respectively. The obtained samples were donated as $x$$SiO_2$–g-$C_3N_4$, where the x presented the amount of added colloidal SiO_2.

Materials characterizations

The morphology of the as-prepared samples was observed by a Regulus 8100 scanning electron microscope (SEM) and a FEI Tecnai F20 transmission electron microscopy (TEM). The element mapping were conducted on an OXFORD XPLORE30 Energy Dispersive Spectrometer operating at an acceleration voltage of 15 kV and using a secondary electron detector. The contents of C, N and O elements were evaluated by an Elementar Vario EL cube elemental analyzer. The amount of residual Si within the g-C_3N_4–O matrix was measured by an Agilent 725 inductively coupled plasma-mass spectrometry. Surface areas and pore size distributions of the photocatalysts were acquired by nitrogen physisorption at 77 K on an ASAP2460 Surface Area and Porosity Analyzer. Fourier transformed infrared (FTIR) spectra were collected using an IRAffinity-1 FTIR spectrometer. Powder X-ray diffraction (XRD) patterns were measured with a D/MAX-2200/PC X-ray diffractometer with Cu Kα radiation at a scanning rate of 5° min^{-1}. The valence states of elements were obtained using a Thermo Scientific K-Alpha X-ray photoelectron spectroscopy (XPS). The wavelength range of visible light adsorption was tested by a on a Shimadzu UV-2550 spectrophotometer in the spectral region of 300–800 nm. The recombination efficiency of photoexcited charge carrier was monitored by a HORIBA Scientific DeltaflexFlex fluorescence lifetime system and a Shimadzu RF-5301PC Luminescence spectrometer.

Photoelectrochemical measurements

Photoelectrochemical measurements were conducted on a CHI760E electrochemical workstation with a standard three-electrode system employing gauze platinum and Ag/AgCl (saturated KCl) as the counter and reference electrode. A slurry was prepared by mixing of 10 mg of as-prepared photocatalyst, 100 μL of Nafion (5 wt%) and 900 μL of ethanol, which was spin coated onto the surface of FTO glass to obtain the working electrode. After air-drying, the working electrode was immersed into a Na_2SO_4 solution (0.5 M) saturated with N_2 and irradiated by a 300 W Xe lamp (PLS-SXE300, Perfect Light). Mott–Schottky plots were recorded at potential range of 0–0.6 V under voltage magnitude of 10 mV and frequency of 1 kHz. The electrochemical impedance spectra (EIS) was measured at

frequency range from 0.1 Hz to 100 kHz under a voltage magnitude of 10 mV.

Computational method and models

All calculations were performed by the Gaussian 16 package based on the density functional theory (DFT). The B3LYP with the 6-311G(d,p) basic set was used for geometries optimization and the Grimme's DFT-D3 method was applied to correct the van der Waals of all molecules. The full width at half maximum was set as 0.2 eV. A minimum g-C_3N_4 trimer with one nitrogen pot was built as the computational model, and its structure was optimized without any symmetry constraints. To investigate the location of the incorporated oxygen, one O atom was introduced into the g-C_3N_4 trimer by replacing one C/N atom. The Multiwfn was employed to analyze the highest occupied molecular orbital (HOMO) and the lowest unoccupied molecular orbital (LUMO) of g-C_3N_4 and g-C_3N_4–O.

Photocatalytic performance measurement

Photocatalytic water splitting towards H_2 generation reactions of the as-prepared photocatalysts were performed in a 500 mL closed quartz reactor under a 300 W Xe lamp irradiation (PLS-SXE300, Perfect Light). The 100 mg of photocatalyst was dispersed in 300 mL aqueous solution containing 10 vol% triethanolamine (TEOA). Before the reaction, the reactor was evacuated to remove dissolved O_2 and bubbled with N_2 until saturation. The light source with a 420 nm cutoff filter was turned on to initiate the photocatalytic reaction and the gaseous products were quantified by a Shimadzu GC-2014 gas chromatograph.

Results and discussion

Powder X-ray diffraction (XRD) patterns of the colloidal SiO_2, bulk g-C_3N_4, and the modified g-C_3N_4 samples synthesized by using varied amount of colloidal SiO_2 were displayed in Fig. 1a. A wide XRD diffraction peak at 22.11° was observed for colloidal SiO_2, which was typical feature of amorphous silica.[35] Compared to the bulk g-C_3N_4, all the modified g-C_3N_4 samples prepared with different amount of colloidal SiO_2 exhibited identical characteristic diffraction peaks at 13.10° and 27.37°, suggesting the complete removal of SiO_2 and the basic heptazine-based structure of as-synthesized samples.[36] The decreased crystallinity of modified g-C_3N_4 sample prepared with 2000 mg colloidal SiO_2 was due to the inhibited condensation in the presence of excess SiO_2.[37] The molecular structures of the colloidal SiO_2, bulk g-C_3N_4 and the modified g-C_3N_4 samples were confirmed by FTIR spectroscopy.

The colloidal SiO_2 presented a strong asymmetric stretching vibration of Si–O–Si band at 1070 cm^{-1} and the characteristic bands of SiO_4 tetrahedra at 796 and 472 cm^{-1} (Fig. 1b).[38] The FTIR spectra of the bulk g-C_3N_4 and modified g-C_3N_4 samples exhibited analogous stretching vibrations of aromatic CN heterocycles at 1200–1700 cm^{-1} and the breathing vibration of heptazine units at 810 cm^{-1} associated with a broad band of terminal –NH_2 in the range of 2800–3500 cm^{-1} (Fig. 1b).[36] The FTIR results demonstrated that the modified g-C_3N_4 samples after the removal of colloidal SiO_2 maintained the intrinsic molecular skeleton of g-C_3N_4.

To verify the composition variation between the bulk g-C_3N_4 and the modified g-C_3N_4 samples, elemental levels of C, N and O for all the samples were analyzed. The samples prepared in three times were measured to obtain the average elemental content within the substrates, as shown in Table 1. In comparison with the relative low oxygen concentration of bulk g-C_3N_4 (1.93 wt%), the amounts of oxygen within the g-C_3N_4 substrate could be tuned from 7.88 to 8.95 wt% by increasing the amount of colloidal SiO_2 added from 500 to 2000 mg. The gradually increased oxygen content of the modified g-C_3N_4 samples illustrated that the selection of colloidal SiO_2 as oxygen source was valid to tune the oxygen concentration of g-C_3N_4. According to the previous work reported, the increased oxygen concentration was contributed by the presence of abundant hydroxyls on the surface of colloidal SiO_2 during the polymerization procedure.[39] Then the modified g-C_3N_4 photocatalysts were concentrated HNO_3 and maintained named as g-C_3N_4–O_x, where x presented the content of oxygen within the matrix. To confirm the content of residual Si element within the g-C_3N_4–O matrix, the photocatalyst was transferred into in polytetrafluoroethylene-lined stainless-steel autoclave at 140 °C for 2 h. No data of Si content was detected in the sample solution, demonstrating the complete removal of colloidal SiO_2 within the g-C_3N_4–O substrate.

The X-ray photoelectron spectroscopy (XPS) and theoretical simulation were conducted to elucidate the elemental state and the location of incorporated oxygen within the g-C_3N_4–O photocatalyst. The survey XPS spectra of bulk g-C_3N_4 and g-C_3N_4–O photocatalysts both confirmed co-existence of C, N and O elements (Fig. 2a). The absence of Si element further confirmed the complete removal of colloidal SiO_2. The C 1s peaks at 284.8,

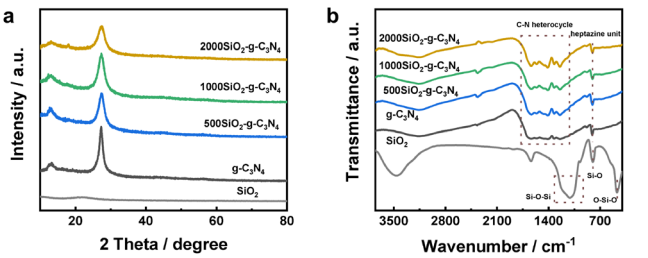

Fig. 1 (a) XRD patterns and (b) FTIR spectra of colloidal SiO_2, bulk g-C_3N_4 and modified g-C_3N_4 samples prepared with different amount of colloidal SiO_2.

Table 1 Elemental analysis of bulk g-C_3N_4 and modified g-C_3N_4 samples prepared with different amount of colloidal SiO_2

Sample	C/wt%	N/wt%	O/wt%
g-C_3N_4	34.34	61.69	1.93
500SiO_2–g-C_3N_4	22.86	45.77	7.88
1000SiO_2–g-C_3N_4	19.97	39.30	8.39
2000SiO_2–g-C_3N_4	26.41	48.36	8.95

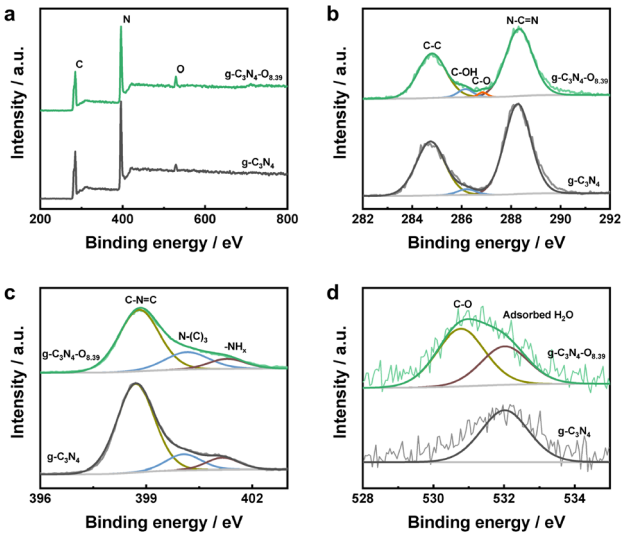

Fig. 2 (a) Survey XPS spectra, (b) high resolution C 1s XPS spectra, (c) high resolution N 1s XPS spectra and (d) high resolution O 1s XPS spectra of bulk g-C_3N_4 and g-C_3N_4–$O_{8.39}$ photocatalysts.

286.2 and 288.3 eV were assigned to the C–C, C–OH and C–N=C groups, respectively (Fig. 2b). New peaks ascribed to C–O bond emerged in the high-resolution C and O 1s XPS spectra of g-C_3N_4–O (Fig. 2b and d), proving the introduced oxygen existed in the form of C–O bond.[40] Combining with the increased C/N mol ratio of all the g-C_3N_4–O samples (0.687–0.709) compared to the bulk g-C_3N_4 (0.649), the introduced oxygen replaced N atoms of the g-C_3N_4 (Table 1). The N 1s peaks centered at 398.8 and 400.2 eV were assigned to C–N=C and N–$(C)_3$ groups (namely, N_{2C} and N_{3C}). The weak N 1s peak at 401.3 eV was ascribed to the terminal –NH_x groups.[34] The bulk g-C_3N_4 and g-C_3N_4–O photocatalysts exhibited identical characteristic peak positions in the high-resolution N 1s XPS spectra (Fig. 2c), implying the elevated concentration of oxygen exerted negligible impact on N species.

While the decreased peak area ratios of N_{2C} to N_{3C} for g-C_3N_4–O (3.48) in comparison with the bulk g-C_3N_4 (5.96) indicated that the substitute of sp^2-hybrided N atoms by incorporated oxygen (Table 2).

Theoretical simulation further confirmed the location of incorporated oxygen atom in the heptazine framework. The model containing a trimer was constructed to represent the repeated heptazine units of g-C_3N_4 (Fig. 3a). One O atom was introduced into the model by substitution of one N atom. The more energy-favorable nitrogen site for O replacement was sp^2-hybrided N site after configuration optimization (Fig. 3b). Results from elemental analysis, XPS measurements combined with theoretical calculations suggested the incorporated oxygen existed in the form of C–O bond by replacing sp^2-hybrided N atom of the heptazine unit.

Table 2 Relative ratios of C–N=C, N–$(C)_3$ and –NH_x determined by high resolution N 1s XPS spectra

	C–N=C		N–$(C)_3$		–NH_x		
Sample	Area	(%)	Area	(%)	Area	(%)	N_{2C}/N_{3C}
g-C_3N_4	42 172	77.23	7072.12	12.95	5362.36	9.82	5.96
g-C_3N_4–O	31 427.28	69.52	9040.26	19.99	4739.98	10.48	3.48

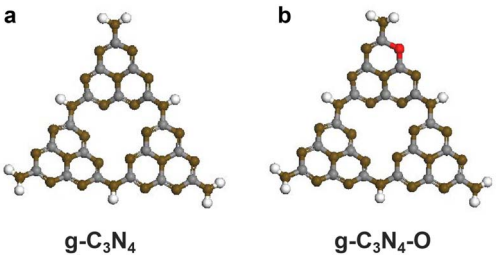

Fig. 3 Optimized structures of (a) g-C_3N_4 trimer and (b) g-C_3N_4–O trimer. The grey, brown, white and red balls represented C, N, H and O atoms, respectively.

The photocatalytic H_2 evolution rate of the bulk g-C_3N_4 and g-C_3N_4–O photocatalysts with different amount of oxygen were evaluated. As shown in Fig. 4a, all the g-C_3N_4–O photocatalysts showed obviously enhanced H_2 evolution rate compared to the bulk g-C_3N_4 (417.2 μmol g^{-1} h^{-1}), indicating that the high oxygen concentration realized by the employment of colloidal SiO_2 could boost the photocatalytic activity of g-C_3N_4 based photocatalyst. When the content of oxygen increased from 7.88 to 8.39 wt%, the H_2 production rate increased from 3475.4 to 4396.8, and then decreased to 2559.2 μmol g^{-1} h^{-1}. This revealed that the photocatalytic H_2 production performance could be tuned through amount regulation of oxygen within the g-C_3N_4 matrix. The recycling stability of g-C_3N_4–O photocatalyst with an optimal content of oxygen (8.39 wt%) was exhibited in Fig. 4b. Its photocatalytic activity maintained after four cycles of H_2 evolution tests, confirming the superior recycling stability of the as-synthesized g-C_3N_4–O photocatalyst.

To understand the mechanism of improved H_2 production performance induced by increased oxygen content, the morphology, porosity, optical and optoelectronic properties of the bulk g-C_3N_4 and g-C_3N_4–O photocatalysts were characterized. The SEM image of colloidal SiO_2 displayed spherical shape with average size of ~50 nm (Fig. 5a). SEM observations showed the typical sheet-like structure of bulk g-C_3N_4 with smooth surface (Fig. 5b). The morphologies of intermediate products

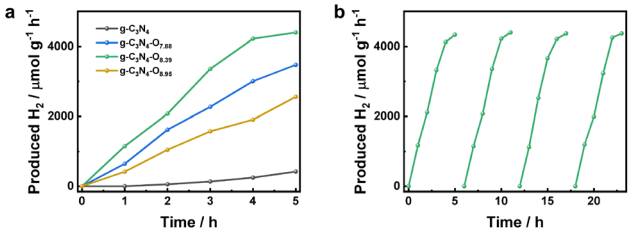

Fig. 4 (a) Photocatalytic H_2 evolution rate of bulk g-C_3N_4 and g-C_3N_4–O photocatalysts with different content of oxygen, (b) cyclic H_2 evolution test of g-C_3N_4–O photocatalyst with an optimal amount of oxygen (8.39 wt%).

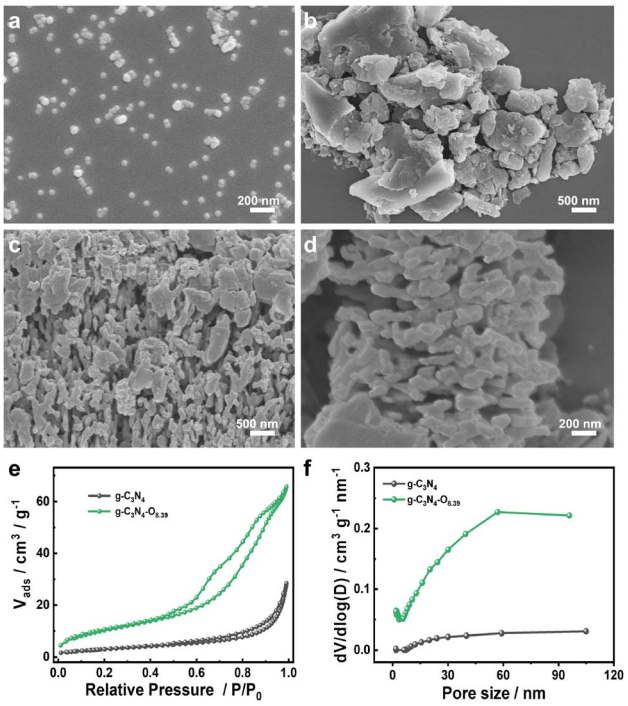

Fig. 5 (a–c) SEM images of (a) colloidal SiO_2, (b) bulk g-C_3N_4 and (c and d) g-C_3N_4–$O_{8.39}$ photocatalysts. (e) Nitrogen adsorption–desorption isotherms and (f) corresponding pore size distribution of bulk g-C_3N_4 and g-C_3N_4–$O_{8.39}$ photocatalysts.

were characterized for understanding the preparation process of the g-C_3N_4–O photocatalyst. After initial drying, phase separation between the silica nanoparticles and DCDA did not occur. It could be seen that the colloidal SiO_2 agglomerated around the DCDA (Fig. S1†). Then the products obtained from the calcination procedure exhibited agglomerated silica nanoparticles dispersed on/around the sheet-like g-C_3N_4 (Fig. S2†). The surface of obtained g-C_3N_4–O after removal of SiO_2 became rough and porous (Fig. 5c and d). The corresponding energy dispersive spectroscopy (EDS) elemental mapping (Fig. S3†) images indicated the successful uniform distribution of C, N and O elements within the g-C_3N_4–O matrix. BET results indicated the mesoporous structure and increased surface area of g-C_3N_4–O photocatalyst (Fig. 5e and f), which was one reason responsible for the improved photocatalytic H_2 production performance.

The optical and optoelectronic properties of g-C_3N_4 with high concentration of oxygen was evaluated by UV-vis diffuse reflectance spectra. The bulk g-C_3N_4 photocatalyst exhibited an absorption edge around 460 nm attributed to semiconductor band–band transition (Fig. 6a). The deeper colour and tail adsorption in the visible light region g-C_3N_4–O photocatalyst showed red-shifted adsorption edge and tail adsorption in the visible light range of 500–800 nm, indicating that the increased oxygen content tail adsorption in the visible light region of g-C_3N_4–O photocatalysts implied enhanced visible light utilization ability, which was favorable for photocatalysis. The PL emission spectra of the samples at an excitation wavelength of 365 nm was shown in Fig. 6b. The decreased PL emission peak

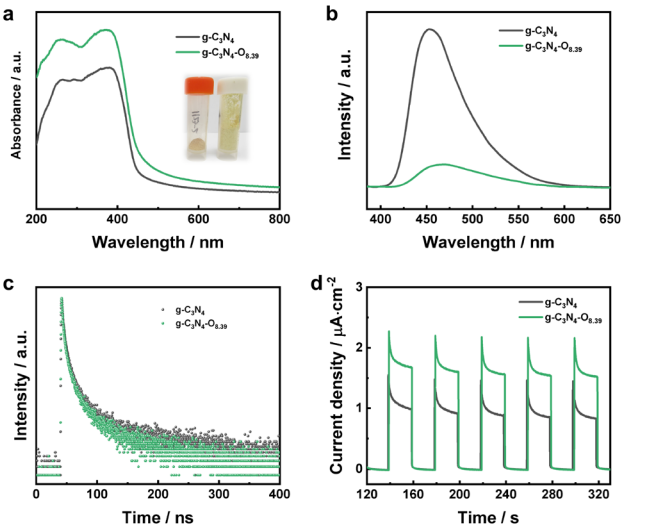

Fig. 6 (a) UV-vis diffusion reflectance spectra (inner pictures: optical pictures of bulk g-C_3N_4 and g-C_3N_4–O samples), (b) PL emission spectra, (c) time-resolved PL decay spectra and (d) periodic photocurrent response of bulk g-C_3N_4 and g-C_3N_4–O photocatalysts.

intensity indicated the decreased recombination rate of photoexcited electron–hole pairs for g-C_3N_4–O photocatalyst. The faster PL decay spectra confirmed the facilitated separation kinetics realized by the increased concentration of oxygen (Fig. 6c).[41,42] This synergistically demonstrated the increased oxygen content promoted photoelectric conversion for H_2O reduction. The periodic photocurrent tests were performed with a light on/off interval of 20 s under open circuit voltage. The enhanced photocurrent density of g-C_3N_4–O photocatalyst implied the migration promotion of photoinduced charge carriers realized by high concentration of oxygen introduction (Fig. 6d).

The optical property of semiconductor photocatalyst was determined by its electronic energy band structure.[43] Thereby, the tauc plots and Mott–Schottky plots were measured to obtain the electronic energy band structure of bulk g-C_3N_4 and g-C_3N_4–O photocatalysts. The band gap of g-C_3N_4 and g-C_3N_4–O photocatalysts were determined to be 2.70 and 2.48 eV from the Tauc plots (Fig. 7a). The high concentration of oxygen induced narrowed band gap and thus red-shifted adsorption edge of g-C_3N_4–O photocatalyst, elevating utilization efficiency of visible light adsorption with longer wavelength. The flat band potentials (E_{fb} *vs.* Ag/AgCl) of the g-C_3N_4 and g-C_3N_4–O photocatalysts were −1.05 and −0.8 V according to the *X* intercept at the

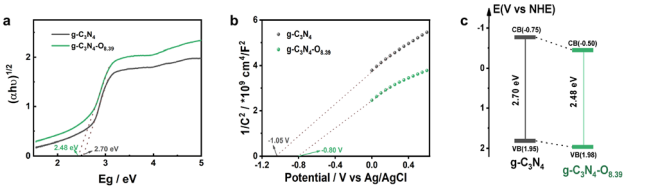

Fig. 7 (a) Tauc plots, (b) Mott–Schottky plots and (c) energy band structure illustration for bulk g-C_3N_4 and g-C_3N_4–O photocatalysts.

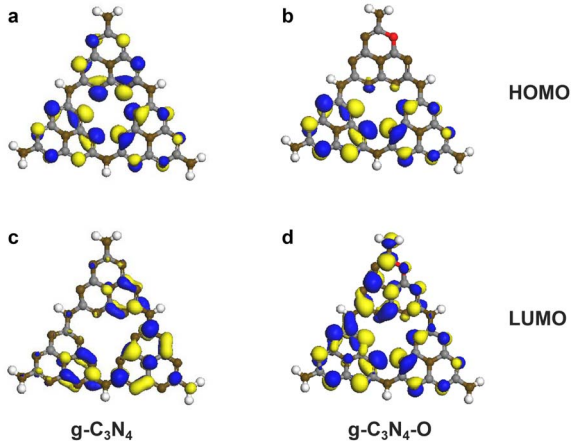

Fig. 8 Calculated HOMO and LUMO for (a and c) bulk g-C_3N_4 and (b and d) g-C_3N_4–O trimer.

tangents of the Mott–Schottky plots (Fig. 7b). The corresponding E_{fb} (*vs.* NHE, pH = 0) potentials of g-C_3N_4 and g-C_3N_4–O photocatalysts were derived to be −0.45 and −0.20 V, respectively.[44] Generally, the E_{fb} potential of the n-type semiconductor was 0.3 V positive than conduction band minimum (CBM) potential.[45] Hence, the CBM potentials of g-C_3N_4 and g-C_3N_4–O photocatalysts were identified to be −0.75 and −0.50 V, respectively. Combining with the E_g values, the valence band minimum (VBM) potentials of the g-C_3N_4 and g-C_3N_4–O photocatalysts were calculated to be 1.95 and 1.98 V, respectively. On the basis of above results, the electronic energy band structures of g-C_3N_4 and g-C_3N_4–O photocatalysts were depicted in Fig. 7c. It could be known that the high concentration of oxygen influenced the energy band potential and narrowed the band gap, accounting for its optimized optical property.

The highest occupied molecular orbital (HOMO) and the lowest unoccupied molecular orbital (LUMO) were calculated to verify the effect of introduced oxygen on the local electron distribution of the π conjugated system (Fig. 8). For the bulk g-C_3N_4, the HOMO is primarily derived from the p_z orbitals of N atoms and the LUMO mainly localized in C–N bond orbitals, which usually resulted in easy recombination of photoexcited electrons and holes.[46,47] The incorporated O atom induced evidently local electron distribution perturbation of HOMO, manifesting in enhanced electron localization located in the oxygen-free subunit. The difference in HOMO and LUMO led to spatial separation of photoexcited electron and holes, accounting for the inhibited recombination of charge carriers for the g-C_3N_4–O photocatalyst. Besides, the O atom within the heptazine unit introduced extra electrons to increase charge density of the π conjugated system. The improved electronic conductivity was responsible for the promoted transportation of charge carriers.

Conclusions

In summary, porous g-C_3N_4 photocatalyst with tunable high concentration of oxygen was synthesized *via* copolymerization of DCDA and colloidal SiO_2. The removal of colloidal SiO_2 contributed to porous structure of g-C_3N_4–O and increased surface area, favoring reactants adsorption and mass transfer. The introduced oxygen by replacement of two-coordinated N atoms narrowed the band gap and disturbed the local electron distribution, thus extended the visible light harvesting and promoted the separation and transportation of photogenerated charge carriers. The obtained g-C_3N_4–O photocatalyst with an optimal oxygen content (8.39 wt%) showed 10.5 times enhancement in H_2 production rate in comparison with bulk g-C_3N_4, attributed to porous structure formation and high concentration of oxygen incorporation. Such work revealed the effect of colloidal SiO_2 on the composition regulation of g-C_3N_4 based photocatalysts.

Conflicts of interest

There are no conflicts to declare.

Acknowledgements

This work was financially supported by the Science and Technology Development Project of Jilin Province (20220101248JC), the 13th Five-Year Science and Technology Project of the Education Department of Jilin Province (JJKH20200124KJ) and the Doctoral Research Start-up Fund of Jilin Medical University (JYBS2021032LK).

References

1 Y. Ping, X. Liu, J. Iocozzia, Y. Yuan, L. Gu, G. Xu and Z. Lin, Highly stable non-noble metal Ni_2P co-catalyst for increased H_2 generation by g-C_3N_4 under visible light irradiation, *J. Mater. Chem. A*, 2017, **5**, 8493–8498.
2 Z. Hui, Y. Dong, P. Jiang, H. Miao and J. Zhang, In situ light-assisted preparation of MoS_2 on graphitic C_3N_4 nanosheets for enhanced photocatalytic H_2 production from water, *J. Mater. Chem. A*, 2015, **3**, 7375–7381.
3 A. Fujishima and K. Honda, Electrochemical photolysis of water at a semiconductor electrode, *Nature*, 1972, **238**, 37–38.
4 L. Ge, C. C. Han, X. L. Xiao, L. L. Guo and Y. J. Li, Enhanced visible light photocatalytic hydrogen evolution of sulfur-doped polymeric g-C_3N_4 photocatalysts, *Mater. Res. Bull.*, 2013, **48**, 3919–3925.
5 Z. Lin, S. J. Wang, Y. Q. Miao, J. P. Yuan, Y. L. Liu, S. G. Xu and S. K. Cao, One-step preparation of halogenated aminobenzonitrile modified g-C_3N_4 via copolymerization and in situ halogen doping for highly enhanced visible light hydrogen evolution, *Int. J. Hydrogen Energy*, 2020, **45**, 6341–6351.
6 J. K. Lin, W. J. Tian, H. Y. Zhang, X. G. Duan, H. Q. Sun and S. B. Wang, Graphitic carbon nitride-based Z-scheme structure for photocatalytic CO_2 reduction, *Energy Fuels*, 2020, **35**, 7–24.
7 K. Z. Qi, Y. B. Xie, R. D. Wang, S. Y. Liu and Z. Zhao, Electroless plating Ni-P cocatalyst decorated g-C_3N_4 with

enhanced photocatalytic water splitting for H_2 generation, *Appl. Surf. Sci.*, 2019, **466**, 847–853.

8 P. Karthika, T. R. N. Kumarab and B. Neppolian, Redox couple mediated charge carrier separation in g-C_3N_4/CuO photocatalyst for enhanced photocatalytic H_2, *Int. J. Hydrogen Energy*, 2020, **45**, 7541–7551.

9 J. Feng, M. M. Gao, Z. Q. Zhang, M. Z. Gu, J. X. Wang, W. J. Zeng and Y. M. Ren, Comparing the photocatalytic properties of g-C_3N_4 treated by thermal decomposition, solvothermal and protonation, *Results Phys.*, 2018, **11**, 331–334.

10 B. R. Bhagat and A. Dashora, Understanding the synergistic effect of co-loading and B-doping in g-C_3N_4 for enhanced photocatalytic activity for overall solar water splitting, *Carbon*, 2021, **178**, 666–677.

11 H. Z. Liu, X. L. Wan, H. Xu and C. X. Luo, Facile synthesis of F-doped g-C_3N_4/$Bi_2Fe_4O_9$ heterostructure with Z-scheme for enhanced photocatalytic performance in NO oxidation, *J. Phys. Chem. Solids*, 2020, **146**, 109500–109506.

12 L. B. Jiang, X. Z. Yuan, Y. Pan, J. Liang, G. M. Zeng, Z. B. Wu and H. Wang, Doping of graphitic carbon nitride for photocatalysis: A review, *Appl. Catal., B*, 2018, **220**, 222–233.

13 H. Starukh and P. Praus, Doping of graphitic carbon nitride with non-metal elements and its applications in photocatalysis, *Catal*, 2020, **10**, 1119–1157.

14 S. Patnaik, D. P. Sahoo and K. Parida, Recent advances in anion doped g-C_3N_4 photocatalysts: A review, *Carbon*, 2021, **172**, 682–711.

15 H. L. Dou, S. H. Zheng and Y. P. Zhang, Graphitic carbon nitride with S and Fe(III) codoping for improved photodegradation performance, *Catal. Lett.*, 2017, **148**, 601–611.

16 C. Ye, J. X. Li, Z. J. Li, X. B. Li, X. B. Fan, L. P. Zhang, B. Chen, C. H. Tung and L. Z. Wu, Enhanced driving force and charge separation efficiency of protonated g-C_3N_4 for photocatalytic O_2 evolution, *ACS Catal.*, 2015, **5**, 6973–6979.

17 Y. O. Wang, H. Suzuki, J. J. Xie, O. Tomita, D. J. Martin, M. Higashi, R. Abe and J. W. Tang, Mimicking natural photosynthesis:solar to renewable H_2 fuel synthesis by Z-scheme water splitting systems, *Chem. Rev.*, 2018, **118**, 5201–5241.

18 K. Pandi, S. K. Lakhera and N. Bernaurdshaw, Efficient promotion and transfer of excited charge carriers in phosphorus doped and Ni complex modified g-C_3N_4, *Catal. Today*, 2021, **370**, 161–172.

19 L. F. Cui, J. L. Song, A. F. McGuire, S. F. Kang, X. Y. Fang, J. J. Wang, C. C. Yin, Y. G. Wang and B. X. Cui, Constructing highly uniform onion-ring-like graphitic carbon nitride for efficient visible-light-driven photocatalytic hydrogen evolution, *ACS Nano*, 2018, **12**, 5551–5558.

20 M. Faisal, A. A. Ismail, F. A. Harraz, S. A. Al-Sayari, A. M. El-Toni, A. E. Al-Salami and M. S. Al-Assiri, Fabrication of highly efficient TiO_2/C_3N_4 visible light driven photocatalysts with enhanced photocatalytic activity, *J. Mol. Struct.*, 2018, **1173**, 428–438.

21 N. I. M. Rosli, S. M. Lam, J. C. Sin, I. Satoshi and A. R. Mohamed, Photocatalytic performance of ZnO/g-C_3N_4 for removal of phenol under simulated sunlight irradiation, *J. Environ. Eng.*, 2018, **144**, 04017091–04017103.

22 J. H. Ma, Z. Q. Wei, L. Li, L. Ma, C. Li and S. P. Huang, Synthesis and photoelectrochemical properties of visible-light response g-C_3N_4@CdS heterojunctions photocatalyst, *Desalin. Water Treat.*, 2021, **231**, 287–296.

23 M. I. Chebanenko, A. A. Lobinsky, V. N. Nevedomskiy and V. I. Popkov, NiO-decorated graphitic carbon nitride toward electrocatalytic hydrogen production from ethanol, *Dalton Trans.*, 2020, **49**, 12088–12097.

24 Z. Feng, L. Zeng, Y. J. Chen, Y. Y. Ma, C. R. Zhao, R. S. Jin, Y. Lu, Y. Wu and Y. M. He, In situ preparation of Z-scheme MoO_3/g-C_3N_4 composite with high performance in photocatalytic CO_2 reduction and RhB degradation, *J. Mater. Res.*, 2017, **32**, 3660–3668.

25 B. Lin, C. Xue, X. Q. Yan, G. D. Yang, G. Yang and B. L. Yang, Facile fabrication of novel SiO_2/g-C_3N_4 core shell nanosphere photocatalysts with enhanced visible light activity, *Appl. Surf. Sci.*, 2015, **357**, 346–355.

26 L. Peng, Z. W. Li, R. R. Zheng, H. Yu and X. T. Dong, Preparation and characterization of mesoporous g-Facile fabrication of novel SiO_2 g-C_3N_4 core shell nanosphere photocatalysts with enhanced visible light activity/SiO_2 material with enhanced photocatalytic activity, *J. Mater. Res.*, 2019, **34**, 1785–1794.

27 S. B. Zhang, M. Li, W. J. Qiu, Y. Wei, G. F. Zhang, J. Y. Han, H. Wang and X. Liu, Super small polymeric carbon nitride nanospheres with core-shell structure for photocatalysis, *ChemistrySelect*, 2017, **2**, 10580–10585.

28 X. Wang, X. Wang X, J. F. Huang, S. X. Li, A. Meng and Z. J. Li, Interfacial chemical bond and internal electric field modulated Z-scheme Sv-$ZnIn_2S_4$/$MoSe_2$ photocatalyst for efficient hydrogen evolution, *Nat. Commun.*, 2021, **12**, 1–11.

29 X. H. Dang, M. S. Xie, F. F. Dai, J. N. Guo, J. Liu and X. Q. Lu, Ultrathin 2D/2D $ZnIn_2S_4$/g-C3N4 nanosheet heterojunction with atomic-level intimate interface for photocatalytic hydrogen evolution under visible light, *Adv. Mater. Interfaces*, 2021, **8**, 2100151–2100164.

30 X. H. Yang, C. Cao, Z. L. Guo, X. Y. Zhang, Y. X. Wang and W. S. Yang, Promoting hydrogen evolution of a g-C_3N_4-based photocatalyst by indium and phosphorus co-doping, *New J. Chem.*, 2021, **45**, 7231–7238.

31 M. Shalom, S. Inal, D. Neher and M. Antoniettia, SiO_2/carbon nitride composite materials: the role of surfaces for enhanced photocatalysis, *Catal. Today*, 2014, **225**, 185–190.

32 Q. Hao, X. X. Niu, C. S. Nie, S. M. Hao, W. Zou, J. M. Ge, D. M. Chen and W. Q. Yao, A highly efficient g-C_3N_4/SiO_2 heterojunction: the role of SiO_2 in the enhancement of visible light photocatalytic activity, *Phys. Chem. Chem. Phys.*, 2016, **18**, 31410–31418.

33 M. T. Xue, G. Q. Tan, T. Liu, L. Lv, B. Li, D. Zhang, M. Y. Dang, H. J. Ren and A. Xia, Insights into the improved photocatalytic performance of fluorine surface modified mpg-C_3N_4 at room temperature under aqueous conditions, *Appl. Catal., A*, 2019, **578**, 89–97.

34 M. S. Akple, T. Ishigaki and P. Madhusudan, Bio-inspired honeycomb-like graphitic carbon nitride for enhanced visible light photocatalytic CO_2 reduction activity, *Environ. Sci. Pollut. Res.*, 2020, **27**, 22604–22618.

35 R. K. Jia, Y. L. Zhang and X. H. Yang, High efficiency photocatalytic CO_2 reduction realized by Ca^{2+} and HDMP group co-modified graphitic carbon nitride, *Int. J. Hydrogen Energy*, 2021, **46**, 32893–32903.

36 B. Lin, S. Chen, F. Dong and G. D. Yang, A ball-in-ball g-C_3N_4@SiO_2 nano-photoreactor for highly efficient H_2 generation and NO removal, *Nanoscale*, 2017, **9**, 5273–5279.

37 X. X. Wang, S. S. Wang, W. D. Hu, J. Cai, L. H. Zhang, L. Z. Dong, L. H. Zhao and Y. M. He, Synthesis and photocatalytic activity of SiO_2/g-C_3N_4 composite photocatalyst, *Mater. Lett.*, 2014, **115**, 53–56.

38 S. Narzary, K. Alamelu, V. Raja and B. M. J. Ali, Visible light active, magnetically retrievable Fe_3O_4@SiO_2@g-C_3N_4/TiO_2 nanocomposite as efficient photocatalyst for removal of dye pollutants, *J. Environ. Chem. Eng.*, 2020, **8**, 104373–104382.

39 M. Q. Xu, B. Chai, J. T. Yan, H. B. Wang, Z. D. Ren and K. W. Paik, Facile synthesis of fluorine doped graphitic carbon nitride with enhanced visible light photocatalytic activity, *Nano*, 2016, **11**, 68–78.

40 F. He, G. Chen, Y. S. Zhou, Y. G. Yu, Y. Zheng and S. Hao, The facile synthesis of mesoporous g-C_3N_4 with highly enhanced photocatalytic H_2 evolution performance, *Chem. Commun.*, 2015, **51**, 16244–16246.

41 F. K. Ma, C. L. Sun, Y. L. Shao, Y. Z. Wu, B. B. Huang and X. P. Hao, One-step exfoliation and fluorination of g-C_3N_4 nanosheets with enhanced photocatalytic activities, *New J. Chem.*, 2017, **41**, 3061–3067.

42 A. Allahresani, B. Taheri and M. A. Nasseri, A green synthesis of spirooxindole derivatives catalyzed by SiO_2@g-C_3N_4 nanocomposite, *New J. Chem.*, 2017, **41**, 3061–3067.

43 G. L. Xu, J. C. Shen, S. M. Chen, Y. J. Gao, H. B. Zhang and J. Zhang, Double defects modified carbon nitride nanosheets with enhanced photocatalytic hydrogen evolution, *Phys. Chem. Chem. Phys.*, 2018, **20**, 17471–17476.

44 W. Wang and J. J. Fang, Mesoporous SiO_2-derived g-C_3N_4@CdS core-shell heteronanostructure for efficient and stable photocatalytic H_2 production, *Ceram. Int.*, 2020, **46**, 2384–2391.

45 X. Yang, Z. Guo, X. Zhang, Y. Han, Z. Xue, T. Xie, *et al.*, The effect of indium doping on the hydrogen evolution performance of g-C_3N_4 based photocatalysts, *New J. Chem.*, 2021, **45**, 544–550.

46 X. Wang, X. Chen, A. Thomas, X. Fu and M. Antonietti, Metal-containing carbon nitride compounds: a new functional organic-metal hybrid material, *Adv. Mater.*, 2009, **21**, 1609–1612.

47 Z. A. Lan, G. Zhang and X. Wang, A facile synthesis of Br-modified g-C_3N_4 semiconductors for photoredox water splitting, *Appl. Catal., B*, 2016, **192**, 116–125.